ISSN 0915-633X

NATIONAL INSTITUTE FOR FUSION SCIENCE

Gyrokinetic Vlasov Code Including Full Three-dimensional Geometry of Experiments

M. Nunami, T.-H. Watanabe and H. Sugama

(Received - Feb. 22, 2010

NIFS-959 Mar. 09, 2010

RESEARCH REPORT
NIFS Series

TOKI, JAPAN

This report was prepared as a preprint of work performed as a collaboration research of the National Institute for Fusion Science (NIFS) of Japan. The views presented here are solely those of the authors. This document is intended for information only and may be published in a journal after some rearrangement of its contents in the future.

Inquiries about copyright should be addressed to the Research Information Office, National Institute for Fusion Science, Oroshi-cho, Toki-shi, Gifu-ken 509-5292 Japan.

E-mail: bunken@nifs.ac.jp

<Notice about photocopying>

In order to photocopy any work from this publication, you or your organization must obtain permission from the following organizaion which has been delegated for copyright for clearance by the copyright owner of this publication.

Except in the USA

Japan Academic Association for Copyright Clearance (JAACC)
6-41 Akasaka 9-chome, Minato-ku, Tokyo 107-0052 Japan
Phone: 81-3-3475-5618 FAX: 81-3-3475-5619 E-mail: jaacc@mtd.biglobe.ne.jp

In the USA

Copyright Clearance Center, Inc.
222 Rosewood Drive, Danvers, MA 01923 USA
Phone: 1-978-750-8400 FAX: 1-978-646-8600

Gyrokinetic Vlasov code including full three-dimensional geometry of experiments

Masanori NUNAMI[1)], Tomo-Hiko WATANABE[1,2)] and Hideo SUGAMA[1,2)]

[1)] *National Institute for Fusion Science, Toki 509-5292, Japan*

[2)] *The Graduate University for Advanced Studies (SOKENDAI), Toki 509-5292, Japan*

A new gyrokinetic Vlasov simulation code, GKV-X, is developed for investigating the turbulent transport in magnetic confinement devices with non-axisymmetric configurations. Effects of the magnetic surface shapes in a three-dimensional equilibrium obtained from the VMEC code are accurately incorporated. Linear simulations of the ion temperature gradient instabilities and the zonal flows in the Large Helical Device (LHD) [O. Motojima, N. Oyabu, A. Komori *et al.*, Nucl. Fusion **43**, 1674 (2003)] configuration are carried out by the GKV-X code for a benchmark test against the GKV code [T.-H. Watanabe and H. Sugama, Nucl. Fusion **46**, 24 (2006)]. The frequency, the growth rate, and the mode structure of the ion temperature gradient instability are influenced by the VMEC geometrical data such as the metric tensor components of the Boozer coordinates for high poloidal wave numbers, while the difference between the zonal flow responses obtained by the GKV and GKV-X codes is found to be small in the core LHD region.

Keywords: gyrokinetic simulation, ITG mode, zonal flow, LHD, VMEC equilibrium

1 Introduction

Anomalous transport of particle, momentum and heat is commonly observed in fusion plasma experiments, and has been a central issue in the magnetic fusion research for the last few decades. It is considered that the anomalous transport is driven by the drift wave plasma turbulence [1], e.g., the ion temperature gradient (ITG) turbulence. The zonal flows are now well known to play a critical role for regulating the turbulent transport in toroidal plasmas, and various works on the zonal flows have been done for tokamaks and stellarator/heliotron configurations [2–4].

Toward the exploration of the zonal flow and the microturbulence in non-axisymmetric configurations, a number of linear and nonlinear gyrokinetic simulations have been performed [5–9]. In our previous papers [6,10], we investigated the effects of single and multiple helicity magnetic field configurations on the ITG turbulence in the helical system by using the gyrokinetic Vlasov flux-tube code, GKV [11]. The simulation results manifest that a neoclassically optimized (inward-shifted) helical configuration leads to a lower level of the ion heat transport through the enhancement of the zonal flows than that in the standard configuration. This is also qualitatively consistent with the Large Helical Device (LHD) [12] experiment results that the anomalous transport is reduced in the inward shifted cases with decreasing the radial drift of ripple trapped particles [13], but increasing the unfavorable field line curvature [14].

For better understandings of the anomalous transport physics, quantitative comparisons between the results of gyrokinetic simulations and experiments are demanded. In the GKV simulations, however, the model helical fields including limited numbers of helical Fourier components are employed with the large aspect ratio approximation to the field geometry, where the Jacobian is assumed to be a constant on the flux-surface, and the diagonal metric tensor components derived from the cylindrical approximation are used. For more quantitative gyrokinetic simulations, thus, it is a natural path to furnish a well established gyrokinetic code with the detailed geometrical information obtained from a three-dimensional equilibrium calculations as in Refs. [15–17]. Being based on this motivation, we developed a new gyrokinetic Vlasov code, GKV-X. The GKV-X code precisely deals with realistic magnetic configuration with full geometrical information given by the VMEC code [18] which is a standard magnetohydrodynamic equilibrium solver for non-axisymmetric systems. Using the GKV-X code, we investigate effects of full geometry of the LHD plasmas on the linear ITG mode and the zonal flow response [6,19–23] by performing the benchmarks with the GKV code.

The rest of this paper is organized as follows. In Sec.2, we briefly summarize field representation and the geometry in the flux coordinate system. In Sec.3, we describe basic equations employed in the GKV and the GKV-X codes, and clarify the differences between the codes for the concrete representations of each term in the equations. In Sec.4, simulation results of the linear ITG instability and the zonal flow response are compared between both codes for investigation of the effects of the metric tensor and the Jacobian in the helical systems. Finally, conclusion is given in Sec.5.

author's e-mail: nunami.masanori@nifs.ac.jp

2 Magnetic field geometry

In this section, for the later use, we describe the detailed expressions of the magnetic field representation and the geometry in flux coordinate systems. Here, we consider the flux coordinate system, $\{\rho, \theta, \zeta\}$, where θ and ζ are poloidal and toroidal angles, respectively. The labeling index of the flux surfaces, $\rho \equiv \sqrt{\Psi/\Psi_a}$, is the dimensionless quantity. Here Ψ represents the toroidal magnetic flux with the minor radius, r, defined by $\Psi = B_{\rm ax} r^2/2$, with the field strength at the magnetic axis, $B_{\rm ax}$, and Ψ_a is the value of the toroidal flux at the last closed surface. Therefore, the flux label can be represented as $\rho = r/a$, where a means the minor radius of the last closed surface defined by $\Psi_a = B_{\rm ax} a^2/2$ at $\rho = 1$.

2.1 Field representation

Let us consider the Boozer coordinates [24], $\{\rho, \theta_{\rm B}, \zeta_{\rm B}\}$, as the flux coordinate system. The contravariant representation of the magnetic field in the Boozer coordinates, is written as

$$\begin{aligned} \boldsymbol{B} &= \nabla\Psi(\rho) \times \nabla\theta_{\rm B} + q^{-1}(\rho)\nabla\zeta_{\rm B} \times \nabla\Psi(\rho) \\ &= \frac{\Psi'}{\sqrt{g_{\rm B}}}\left(\boldsymbol{e}_{\zeta_{\rm B}} + q^{-1}(\rho)\boldsymbol{e}_{\theta_{\rm B}}\right) \\ &= B^{\zeta_{\rm B}}\boldsymbol{e}_{\zeta_{\rm B}} + B^{\theta_{\rm B}}\boldsymbol{e}_{\theta_{\rm B}}, \end{aligned} \tag{1}$$

where, $\boldsymbol{e}_{\theta_{\rm B}} \equiv \partial\boldsymbol{r}/\partial\theta_{\rm B}$, $\boldsymbol{e}_{\zeta_{\rm B}} \equiv \partial\boldsymbol{r}/\partial\zeta_{\rm B}$, $q(\rho)$ is the safety factor and $\sqrt{g_{\rm B}}$ is the Jacobian in the coordinate system,

$$\begin{aligned} \sqrt{g_{\rm B}} &= \left(\nabla\rho \times \nabla\theta_{\rm B} \cdot \nabla\zeta_{\rm B}\right)^{-1} \\ &= \frac{\Psi'}{B^2}\left(B_{\zeta_{\rm B}} + q^{-1}(\rho)B_{\theta_{\rm B}}\right), \end{aligned} \tag{2}$$

where the prime symbol represents the derivative with respect to the flux label ρ, i.e., $A' = dA/d\rho$. Hereafter, for simplicity, the subscript 'B' of the poloidal and toroidal angles is suppressed when the angles are used as subscripts of any variables, e.g., $B_{\theta_{\rm B}}$ is rewritten by B_θ. The poloidal and toroidal covariant components of the field, B_θ and B_ζ, are flux functions in the Boozer coordinates, and consist of the covariant representation of the field written as

$$\boldsymbol{B} = B_\rho\nabla\rho + B_\theta\nabla\theta_{\rm B} + B_\zeta\nabla\zeta_{\rm B}. \tag{3}$$

The components of the equilibrium field, B_θ, B_ζ, B^θ and B^ζ are directly given by VMEC code except for the component B_ρ. The radial covariant component B_ρ can be determined using the contravariant ones,

$$B_\rho = B^\theta g_{\theta\rho} + B^\zeta g_{\zeta\rho}. \tag{4}$$

Here, $g_{\theta\rho}$ and $g_{\zeta\rho}$ are the covariant components of the metric tensor which are given in the next subsection.

2.2 Metric components

Since the VMEC code uses the original coordinate system, so-called "VMEC coordinates", we need to convert the coordinates into the Boozer coordinates. For the purpose, we use the NEWBOZ code [25] which transforms coordinates from the VMEC to the Boozer coordinates $\{\rho, \theta_{\rm B}, \zeta_{\rm B}\}$ with the radial flux label ρ. The VMEC/NEWBOZ code package outputs the information for the shapes of the flux surfaces defined in the cylindrical coordinates $\{R, Z, \phi\}$ as Fourier series for $\theta_{\rm B}$ and $\zeta_{\rm B}$,

$$\begin{aligned} R &= \sum_k R_k(\rho)\cos(n_k\zeta_{\rm B} - m_k\theta_{\rm B}), \\ Z &= \sum_k Z_k(\rho)\sin(n_k\zeta_{\rm B} - m_k\theta_{\rm B}), \\ \phi &= \zeta_{\rm B} + \sum_k \phi_k(\rho)\sin(n_k\zeta_{\rm B} - m_k\theta_{\rm B}). \end{aligned} \tag{5}$$

From Eq.(5), the covariant metric components can be obtained,

$$g_{ij} = \frac{\partial R}{\partial i}\frac{\partial R}{\partial j} + \frac{\partial Z}{\partial i}\frac{\partial Z}{\partial j} + R^2\frac{\partial\phi}{\partial i}\frac{\partial\phi}{\partial j}, \tag{6}$$

where $i, j = \{\rho, \theta_{\rm B}, \zeta_{\rm B}\}$. Making use of Eqs.(1), (2) and (3), $g_{\theta\zeta}$ and $g_{\zeta\zeta}$ can also be represented in a different form,

$$\begin{aligned} g_{\theta\zeta} &= \frac{\sqrt{g_{\rm B}}}{\Psi'}B_\theta - q^{-1}(\rho)g_{\theta\theta}, \\ g_{\zeta\zeta} &= \frac{\sqrt{g_{\rm B}}}{\Psi'}B_\zeta - q^{-1}(\rho)g_{\theta\zeta}, \end{aligned} \tag{7}$$

which are useful for consistency check of the calculation of the metric tensor. We can obtain the contravariant metric components from the covariant ones,

$$g^{il} = \frac{1}{g_{\rm B}}\left(g_{jm}g_{kn} - g_{jn}g_{km}\right), \tag{8}$$

where $\{i, j, k\}$ and $\{l, m, n\}$ are even permutations of $\{\rho, \theta_{\rm B}, \zeta_{\rm B}\}$. In Fig.1, we show an example of the contravariant components of the metric tensor in the standard LHD equilibrium at the flux label $\rho = 0.6$, where g^{ij} for $i, j = \{\rho, \theta_{\rm B}, \zeta_{\rm B}\}$ calculated from the VMEC/NEWBOZ output are plotted along the field line.

3 GKV and GKV-X codes

In the present section, we give the gyrokinetic equation employed in the GKV and the GKV-X codes, and present concrete expressions of each term of which profiles along the field line are compared for the two codes.

3.1 Basic equations

Let $\{r, \theta, \zeta\}$ be a generalized flux coordinate system. The local flux-tube model [26] with the field-aligned

coordinates, $\{x, y, z\}$, is used in the codes, where $x = r - r_0$, $y = (r_0/q_0)\,[q(\rho)\theta - \zeta]$ and $z = \theta$, with the safety factor q_0 at the minor radius $r_0 = \rho_0 a$. The minor radius, r_0, is defined by the toroidal magnetic flux $\Psi(r = r_0) = B_{\rm ax} r_0^2/2$. The both codes solve the electrostatic gyrokinetic equation of the perturbed ion gyrocenter distribution function δf [11, 27],

$$\frac{\partial \delta f}{\partial t} + v_{||}\boldsymbol{b}\cdot\nabla\delta f + \frac{c}{B_0}\boldsymbol{b}\times\nabla\Phi\cdot\nabla\delta f + \boldsymbol{v}_{\rm d}\cdot\nabla\delta f - \frac{\mu}{m_{\rm i}}\boldsymbol{b}\cdot\nabla B\frac{\partial \delta f}{\partial v_{||}} = \left(\boldsymbol{v}_* - \boldsymbol{v}_{\rm d} - v_{||}\boldsymbol{b}\right)\cdot\frac{e\nabla\Phi}{T_{\rm i}}F_{\rm M} + C(\delta f), \quad (9)$$

where $\boldsymbol{b} = \boldsymbol{B}/B$ is the unit vector parallel to the magnetic field, $v_{||}$ and $\mu = m_{\rm i}v_\perp^2/2B$, which are regarded as the velocity-space coordinates in the codes, denotes the parallel velocity and the magnetic moment, respectively. The Maxwellian distribution with the temperature $T_{\rm i}$ and the collision term are denoted by $F_{\rm M}$ and $C(\delta f)$, respectively. The magnetic drift velocity is $\boldsymbol{v}_{\rm d} = (c/eB)\boldsymbol{b}\times(\mu\nabla B + m_{\rm i}v_{||}^2\boldsymbol{b}\cdot\nabla\boldsymbol{b})$ and the diamagnetic drift velocity, $\boldsymbol{v}_* = (cT_{\rm i}/eB)\boldsymbol{b}\times[\nabla\ln n + (m_{\rm i}v^2/2T_{\rm i} - 3/2)\nabla\ln T_{\rm i}]$. The perpendicular wave number vector is defined by

$$\boldsymbol{k}_\perp = k_x\nabla r + k_y\nabla\left[\frac{r_0}{q_0}\left(q(r)\theta - \zeta\right)\right]. \quad (10)$$

In the wave number space, (k_x, k_y), the average electrostatic potential at the gyrocenter, Φ, is related to the electrostatic potential at the particle position, ϕ, as $\Phi_{k_x,k_y} = J_0(k_\perp v_\perp/\Omega_{\rm i})\phi_{k_x,k_y}$. The zeroth-order Bessel function, $J_0(k_\perp v_\perp/\Omega_{\rm i})$, represents the finite gyroradius effect, where the ion gyro frequency is defined by $\Omega_{\rm i} = eB/m_{\rm i}c$. The electrostatic potential ϕ_{k_x,k_y} is calculated from the quasi-neutrality condition,

$$\int d^3v J_0\delta f_{k_x,k_y} - n_0\frac{e\phi_{k_x,k_y}}{T_{\rm i}}\left[1 - \Gamma_0(b)\right] = n_{{\rm e},k_x,k_y}, \quad (11)$$

where $\delta f_{k_x,k_y}$ is the Fourier component of δf, $\Gamma_0(b) = e^b I_0(b)$ with $b = (k_\perp v_{\rm ti}/\Omega_{\rm i})^2$, and I_0 is the modified zeroth-order Bessel function. The ion thermal speed is defined by $v_{\rm ti} = \sqrt{T_{\rm i}/m_{\rm i}}$. The electron density perturbation, $n_{{\rm e},k_x,k_y}$, is assumed to be adiabatic, and is given in terms of the electron temperature, T_e, and the averaged density, n_0, by

$$\frac{n_{{\rm e},k_x,k_y}}{n_0} = \begin{cases} e\left[\phi_{k_x,k_y} - \langle\phi_{k_x,k_y}\rangle\right]/T_{\rm e} & \text{if } k_y = 0, \\ e\phi_{k_x,k_y}/T_{\rm e} & \text{if } k_y \neq 0. \end{cases} \quad (12)$$

Also, $\langle\cdots\rangle$ means the flux surface average written as

$$\langle A(z)\rangle = \int_{-\infty}^{\infty}\sqrt{g_{\rm F}}A(z)dz\Big/\int_{-\infty}^{\infty}\sqrt{g_{\rm F}}dz, \quad (13)$$

for arbitrary function of z, $A(z)$. Here, $\sqrt{g_{\rm F}}$ is the Jacobian in the coordinate system, $\{x, y, z\}$, which has the relation with the Jacobian in the Boozer coordinates, Eq.(2),

$$\sqrt{g_{\rm F}} = \frac{q_0}{ar_0}\sqrt{g_{\rm B}}. \quad (14)$$

We adopt the modified periodic boundary condition at the boundaries of the flux-tube domain [26]. In the linear and collisionless case, the Fourier transformed expression of Eq.(9) becomes

$$\left(\frac{\partial}{\partial t} + v_{||}\boldsymbol{b}\cdot\nabla - \frac{\mu}{m_{\rm i}}\boldsymbol{b}\cdot\nabla B\frac{\partial}{\partial v_{||}} + i\omega_{\rm Di}\right)\delta f_{k_x,k_y} = F_{\rm M}(-v_{||}\boldsymbol{b}\cdot\nabla - i\omega_{\rm Di} + i\omega_{*T{\rm i}})J_0(k_\perp\rho_{\rm i})\frac{e\phi_{k_x,k_y}}{T_{\rm i}}, \quad (15)$$

where $\omega_{\rm Di} = \boldsymbol{k}_\perp\cdot\boldsymbol{v}_{\rm d}$ and $\omega_{*T{\rm i}} = \boldsymbol{k}_\perp\cdot\boldsymbol{v}_*$ are the magnetic and diamagnetic drift frequencies, respectively, and the ion gyroradius is defined by $\rho_{\rm i} = v_\perp/\Omega_{\rm i}$.

3.2 Geometrical expressions used in GKV

In the GKV simulations for the helical configurations such as the LHD, we employed model field configuration,

$$B = B_0\Big[1 - \epsilon_{00}(r) - \epsilon_{\rm t}(r)\cos\theta - \sum_{l=L-1}^{L+1}\epsilon_l(r)\cos\left[l\theta - M\zeta\right]\Big], \quad (16)$$

which includes the toroidal $\epsilon_{\rm t}$, main helicity $\epsilon_{\rm h} = \epsilon_L$, and two side-band helical components $\epsilon_+ = \epsilon_{L+1}$ and $\epsilon_- = \epsilon_{L-1}$. Here, M and L mean the main period numbers of the confinement field in the toroidal and poloidal directions, respectively. For the LHD, $L = 2$ and $M = 10$. Here, we regard the poloidal angle θ as a coordinate along the field line labeled by $\alpha = \zeta - q_0\theta = \text{const}$. In the GKV code, we employ the large aspect ratio approximation for the confinement field geometry assuming small helical ripples and cylindrical diagonal metric tensor [7, 8]. Under the approximation, in terms of the field-aligned coordinates $\{x, y, z\}$, the magnetic drift frequency in the right hand side of Eq.(15) is given by

$$\omega_{\rm Di} = -\frac{c}{e}\left(\mu + \frac{1}{B}m_{\rm i}v_{||}^2\right)\frac{\epsilon_{\rm t}}{r_0} \times\Bigg[k_y\Big(\frac{\rho_0\epsilon_{00}'}{\epsilon_{\rm t}} + \frac{\rho_0\epsilon_{\rm t}'}{\epsilon_{\rm t}}\cos z + \sum_{l=L-1}^{L+1}\frac{\rho_0\epsilon_l'}{\epsilon_{\rm t}}\cos[(l - Mq_0)z - M\alpha]\Big) + (k_x + \hat{s}zk_y)\Big(\sin z + \sum_{l=L-1}^{L+1}l\frac{\epsilon_l}{\epsilon_{\rm t}}\sin[(l - Mq_0)z - M\alpha]\Big)\Bigg], \quad (17)$$

using Eq.(16) for a fixed α. Here, $\hat{s} = (r_0/q_0)dq/dr = (\rho_0/q_0)q'$ is the magnetic shear parameter which is assumed to be constant, and $\epsilon' = d\epsilon/d\rho = a(d\epsilon(r)/dr)$ is used. The diamagnetic drift frequency is expressed as

$$\omega_{*T\mathrm{i}} = -\frac{cT_\mathrm{i}}{eB_0L_n}k_y\left[1+\eta_\mathrm{i}\left(\frac{m_\mathrm{i}v^2}{2T_\mathrm{i}}-\frac{3}{2}\right)\right], \quad (18)$$

where $\eta_\mathrm{i} = L_n/L_T$ with the background gradients for the density, $L_n^{-1} = -d\ln n/dr$, and for the temperature, $L_T^{-1} = -d\ln T_\mathrm{i}/dr$. The perpendicular wave number $k_\perp$ is written as

$$k_\perp^2 = (k_x + \hat{s}zk_y)^2 + k_y^2, \quad (19)$$

which is used for the zeroth-order Bessel function in Eq.(15) and the zeroth-order modified Bessel function in Eq.(11). The parallel derivative in Eq.(15) is given by

$$\boldsymbol{b}\cdot\nabla = \frac{1}{R_0q_0}\frac{\partial}{\partial z}, \quad (20)$$

where the safety factor q_0 and the major radius R_0 are regarded as constant. This corresponds to the approximation that the Jacobian is expressed as $\sqrt{g_\mathrm{F}} \propto 1/(\boldsymbol{B}\cdot\nabla\theta) \propto 1/B$, namely, $B\sqrt{g_\mathrm{F}}$ is a constant on the flux surface. This implies that the coordinates in this model does not coincide with the Boozer coordinates, exactly. In the large aspect ratio approximation, however, the difference is entirely small. The flux surface average for arbitrary function, $A(z)$, in Eq.(13) reduces to

$$\langle A(z)\rangle = \int_{-\infty}^{\infty}A(z)dz/B \Big/ \int_{-\infty}^{\infty}dz/B, \quad (21)$$

which guarantees the property, $\langle \boldsymbol{B}\cdot\nabla A\rangle = 0$. According to the approximation, the parallel derivative of B, which is employed for the mirror force term in Eq.(15), can be written as

$$\boldsymbol{b}\cdot\nabla B = \frac{B_0\epsilon_\mathrm{t}}{R_0q_0}\left(\sin z + \sum_{l=L-1}^{L+1}(l-Mq_0)\frac{\epsilon_l}{\epsilon_\mathrm{t}}\sin[(l-Mq_0)z - M\alpha]\right), \quad (22)$$

with the constant field line label α.

3.3 Geometrical expressions used in GKV-X

In the new code, GKV-X, we employ the same basic equations as the GKV code, Eq.(9) and (11), but with the confinement field model obtained by the VMEC/NEWBOZ code package which outputs the confinement field strength in terms of the Fourier series in the Boozer coordinate system, $\{\rho, \theta_\mathrm{B}, \zeta_\mathrm{B}\}$,

$$B = \sum_{n=0}^{n_{\max}}B_{0,n}(\rho)\cos n\zeta_\mathrm{B} + \sum_{m=1}^{m_{\max}}\sum_{n=-n_{\max}}^{n_{\max}}B_{m,n}(\rho)\cos[m\theta_\mathrm{B} - n\zeta_\mathrm{B}], \quad (23)$$

where $B_{m,n}(\rho)$ is the Fourier component with the poloidal (m) and the toroidal (n) mode numbers. Here, $m_{\max}$ and $n_{\max}$ are the maximum mode numbers for poloidal and toroidal directions used in the VMEC calculation. In the GKV-X, furthermore, we implement exact representations of each term in Eq.(9) with full geometrical factors, the Jacobian and the metric tensor. In the coordinates, $\{\rho, \theta_\mathrm{B}, \zeta_\mathrm{B}\}$, the magnetic drift frequency in Eq.(15) with zero-beta, $\boldsymbol{b}\cdot\nabla\boldsymbol{b} = (\nabla_\perp B)/B$, is given by

$$\begin{aligned}\omega_\mathrm{Di} = &-\frac{c}{eB^2}\frac{a}{\sqrt{g_\mathrm{B}}}\left(\mu+\frac{1}{B}m_\mathrm{i}v_\parallel^2\right)\\ &\times\left[k_y\left\{\left(\frac{\rho_0}{q_0}B_\rho+\hat{s}\theta_\mathrm{B}B_\zeta\right)\frac{\partial B}{\partial\theta_\mathrm{B}}\right.\right.\\ &\quad+(\rho_0B_\rho-\hat{s}\theta_\mathrm{B}B_\theta)\frac{\partial B}{\partial\zeta_\mathrm{B}}\\ &\quad\left.-\left(\frac{\rho_0}{q_0}B_\theta+\rho_0B_\zeta\right)\frac{\partial B}{\partial\rho}\right\}\\ &\left.+k_x\left\{B_\zeta\frac{\partial B}{\partial\theta_\mathrm{B}}-B_\theta\frac{\partial B}{\partial\zeta_\mathrm{B}}\right\}\right], \end{aligned} \quad (24)$$

with the perpendicular wave numbers, k_x and k_y, where the field-aligned coordinates, $\{x, y, z\}$, for the GKV-X case are defined later. The diamagnetic drift frequency can also be expressed as

$$\begin{aligned}\omega_{*T\mathrm{i}} &= -\frac{cT_\mathrm{i}}{eL_n}\frac{\rho_0a^2}{q_0B^2\sqrt{g_\mathrm{B}}}(B_\theta+q_0B_\zeta)\\ &\quad\times k_y\left[1+\eta_\mathrm{i}\left(\frac{m_\mathrm{i}v^2}{2T_\mathrm{i}}-\frac{3}{2}\right)\right]\\ &= -\frac{cT_\mathrm{i}}{eL_n}\frac{\rho_0a^2}{\Psi'}k_y\left[1+\eta_\mathrm{i}\left(\frac{m_\mathrm{i}v^2}{2T_\mathrm{i}}-\frac{3}{2}\right)\right], \end{aligned} \quad (25)$$

where we use Eq.(2) in the last line. Using the identity for the contravariant components of the metric tensor, Eq.(8), we can obtain the perpendicular wave number $k_\perp$ as follows;

$$\begin{aligned}k_\perp^2 &= k_x^2a^2g^{\rho\rho}\\ &+ 2k_xk_ya^2\left[\hat{s}\theta_\mathrm{B}g^{\rho\rho}+\frac{\rho_0}{q_0}\left(q_0g^{\rho\theta}-g^{\rho\zeta}\right)\right]\\ &+ k_y^2a^2\left[\frac{\rho_0^2}{q_0^2}\left(g^{\zeta\zeta}+q_0^2g^{\theta\theta}-2q_0g^{\theta\zeta}\right)\right.\\ &+ \left.2\hat{s}\theta_\mathrm{B}\frac{\rho_0}{q_0}\left(q_0g^{\rho\theta}-g^{\rho\zeta}\right)+\hat{s}^2\theta_\mathrm{B}^2g^{\rho\rho}\right]. \end{aligned} \quad (26)$$

The parallel derivative is determined as

$$\boldsymbol{b}\cdot\nabla = \frac{\Psi'}{q_0B\sqrt{g_\mathrm{B}}}\left(\frac{\partial}{\partial\theta_\mathrm{B}}+q_0\frac{\partial}{\partial\zeta_\mathrm{B}}\right), \quad (27)$$

with the Jacobian Eq.(2). Therefore, in the GKV-X code, we use Eq.(13) as the flux surface averaging, and

the parallel derivative of B can be represented as

$$\boldsymbol{b}\cdot\nabla B = \frac{\Psi'}{q_0 B\sqrt{g_{\rm B}}} \times \sum_{m=1}^{m_{\rm max}}\sum_{n=n_{\rm max}}^{n_{\rm max}} B_{m,n}(\rho)(m-nq_0)\sin[n\zeta_{\rm B}-m\theta_{\rm B}]. \tag{28}$$

In Eq.(24), we use derivatives of the field strength along each direction in the coordinates $\{\rho,\theta_{\rm B},\zeta_{\rm B}\}$ written by

$$\begin{aligned}
\frac{\partial B}{\partial\rho} &= \sum_{n=0}^{n_{\rm max}} B'_{0,n}(\rho)\cos n\zeta_{\rm B} \\
&+ \sum_{m=1}^{m_{\rm max}}\sum_{n=-n_{\rm max}}^{n_{\rm max}} B'_{m,n}(\rho)\cos[m\theta_{\rm B}-n\zeta_{\rm B}], \\
\frac{\partial B}{\partial\theta_{\rm B}} &= \sum_{m=1}^{m_{\rm max}}\sum_{n=-n_{\rm max}}^{n_{\rm max}} B_{m,n}(\rho)m\sin[n\zeta_{\rm B}-m\theta_{\rm B}], \\
\frac{\partial B}{\partial\zeta_{\rm B}} &= -\sum_{n=0}^{n_{\rm max}} B_{0,n}(\rho)n\sin n\zeta_{\rm B} \\
&+ \sum_{m=1}^{m_{\rm max}}\sum_{n=-n_{\rm max}}^{n_{\rm max}} B_{m,n}(\rho)n\sin[m\theta_{\rm B}-n\zeta_{\rm B}].
\end{aligned} \tag{29}$$

In the GKV-X code, we use above terms after we convert the coordinates into the field-aligned coordinates $\{x,y,z\}$ with the relations, $x=a(\rho-\rho_0)$, $y=(a\rho_0/q_0)(q\theta_{\rm B}-\zeta_{\rm B})$ and $z=\theta_{\rm B}$ in a constant field line label $\alpha=\zeta_{\rm B}-q_0\theta_{\rm B}$. The parallel derivative in Eq.(27), for example, is written as $\boldsymbol{b}\cdot\nabla=(\Psi'/q_0B\sqrt{g_{\rm B}})(\partial/\partial z)$. The concrete profiles of each term in the equation (15), which are used in the GKV and the GKV-X simulation, are shown in Fig.2. The details of the profiles are discussed in the next section.

4 Comparison of simulation results

In order to investigate the effects of non-axisymmetric geometry on the ITG modes and zonal flows, gyrokinetic Vlasov simulations by linearized versions of the GKV-X and the GKV codes are performed in a similar way as in Refs. [7] and [11]. Here, we use the magnetic configuration with the parameters of the confinement field based on the VMEC calculation results for the standard LHD case which is similar to 'S-B case' in Ref. [8]. In the GKV-X simulation, we use the VMEC configuration with full helical components. On the other hand, the GKV calculation utilizes the parameters summarized in Table 1 which are obtained from the VMEC configuration in terms of the toroidal, main helical, two side-band components and their radial derivatives. In both calculations, we use same parameters for the variables, $\eta_{\rm i}=3$, $T_{\rm e}/T_{\rm i}=1$, $L_n/R_0=0.3$, $q_0=1.9$, $\hat{s}=-0.87501$ and $\alpha=0$.

4.1 Effects of full geometry

To highlight differences in the effects of the metric tensor, the Jacobian and full Fourier components of the confinement field between the two models, we plot profiles of each term in Eq.(15), of which concrete expressions are described in the previous section. In Fig.2, we plot the normalized field strength, the magnetic drift frequency, $\omega_{\rm Di}$, normalized by $v_{\rm ti}L_n^{-1}$, the mirror force term, $(\mu/m_{\rm i})\boldsymbol{b}\cdot\nabla B$, normalized by $v_{\rm ti}^2L_n^{-1}$, and the square of the normalized perpendicular wave number, $k_\perp\rho_{\rm i}$, as functions of the field-aligned coordinate z at $\rho=0.6$. Here, for the normalization of the field strength, we use $B_{0,0}(\rho)$ as the normalization factor B_0. As seen in the figures, the profiles of the field strengths, the magnetic drift frequencies, and the mirror force terms for the GKV-X and the GKV codes look very similar to each other. However, in the region near $z=0$, where the ITG instabilities are driven stronger because of more unfavorable magnetic field line curvature, a difference in the magnitude of the magnetic drift frequencies is not negligible, and actually causes a difference in the ITG-mode growth rates. For the diamagnetic drift frequency given in Eqs.(18) and (25), we find that they have only a small difference by the factor of $\omega_{*T{\rm i}}^{\rm (GKV)}/\omega_{*T{\rm i}}^{\rm (GKV\text{-}X)}=\Psi'/(a^2\rho_0B_0)\simeq 1.0097$. The profiles of the perpendicular wave number show an obvious difference due to the effects of the helical ripples on the metric tensor. In the following simulations for the linear ITG modes and collisionless damping of the zonal flows, we obtain the results at $\rho=0.6$ which is in core plasma region of the LHD.

4.2 Linear ITG instability

Figure 3 shows growth rates and real frequencies of the linear ITG instability, obtained from the GKV-X and the GKV simulations for $\rho=0.6$, as functions of the normalized poloidal wave number $k_y\rho_{\rm i}$, where $k_x=0$ is used. The growth rate in the GKV-X calculation is slightly higher than the GKV results for $k_y\rho_{\rm i}\lesssim 0.3$ and lower for $k_y\rho_{\rm i}\gtrsim 0.3$. The real frequency given by the GKV-X simulation is slightly more negative than the GKV result. The differences between the codes are magnified as the poloidal wave number increases, which originates from the ripple components and the full metric tensor through the magnetic drift frequency ($\omega_{\rm Di}$) and the perpendicular wave number ($k_\perp$), respectively. Since more helical ripple components are included in the magnetic drift frequency for the GKV-X case, the difference of $\omega_{\rm Di}$ appears as seen in Fig.2-(b), that is, $\omega_{\rm Di}$ for the GKV-X is more negative than for the GKV around $z\simeq 0$ where the ITG instabilities are strongly driven because of unfavorable magnetic field line curvature. According to Eq.(24), the difference in $\omega_{\rm Di}$ is enhanced in the large $|k_y|$ region. In the expression of the perpendicular wave number, Eq.(26), the terms including the metric tensor com-

ponents $g^{\theta\theta}$ and $g^{\rho\rho}$, which reflect the shape of the elliptic magnetic surface, are influential in $k_\perp$ related to the finite gyroradius effect. The term with $g^{\theta\theta}$ remains finite around $z \simeq 0$, and the contribution of the term to $k_\perp$ is also enhanced for higher poloidal wave numbers, while the term with $g^{\rho\rho}$ vanishes at $z = 0$. In the other terms of Eq.(15), i.e., the diamagnetic drift frequency and the mirror force term, the differences between the codes are much smaller than those in $\omega_{\rm Di}$ and $k_\perp$. Therefore, at large poloidal wave numbers, the helical ripple components of the confinement field and the metric tensor of the magnetic surface affect the frequency and the growth rate of the ITG instability, through the magnetic drift frequency and the finite gyroradius effect.

Eigenfunctions of the ITG modes are also investigated as shown in Fig.4 for $k_y\rho_{\rm i} = 0.324$ and $k_y\rho_{\rm i} = 0.649$. As seen in the plot for $k_y\rho_{\rm i} = 0.324$, the mode structures of ϕ_k obtained by the two codes have a similar profile which is accompanied by oscillations associated with the helical ripples. In contrast, the field-aligned profiles of ϕ_k for larger poloidal wave number $k_y\rho_{\rm i} = 0.649$ show different ripple structures in the unfavorable curvature region around $z \simeq 0$. This is consistent with the results of the growth rate and the real frequency shown in Fig.3, where the differences are mainly found in the higher poloidal wave numbers. Linear eigenvalue analysis [28–30] also predict the similar mode structure to the present results.

4.3 Zonal flow evolution

The zonal flows are produced by an electrostatic field perturbation varying in the radial direction, and have the poloidal wave number $k_y = 0$. Hence, the perpendicular wave numbers in Eq.(19) and Eq.(26) are simply given by

$$k_\perp^2 = \begin{cases} k_x^2 & \text{for GKV,} \\ k_x^2 a^2 g^{\rho\rho} & \text{for GKV-X.} \end{cases} \tag{30}$$

Figure 5 shows the time evolution of the flux surface averaged zonal flow potential $\langle \phi_{k_\perp} \rangle$ during their linear collisionless damping found in the GKV and the GKV-X simulations. The results are shown for two different radial wave numbers, $k_x\rho_{\rm i} = 0.0637$ and $k_x\rho_{\rm i} = 0.1274$. As seen in the plots, the response functions of the zonal flows to the initial perturbation, $\langle \phi_{k_\perp}(t) \rangle / \langle \phi_{k_\perp}(0) \rangle$ given by the two codes agree well with each other for both k_x. The residual levels of the zonal flow potentials at $t/(L_n/v_{\rm ti}) = 100$ are obtained as $\mathcal{K}_{\text{GKV-X}} = (1.33 \pm 0.81) \times 10^{-2}$, $\mathcal{K}_{\rm GKV} = (1.32 \pm 0.79) \times 10^{-2}$ for $k_x\rho_{\rm i} = 0.0637$, and $\mathcal{K}_{\text{GKV-X}} = (3.54 \pm 0.15) \times 10^{-2}$, $\mathcal{K}_{\rm GKV} = (3.36 \pm 0.10) \times 10^{-2}$ for $k_x\rho_{\rm i} = 0.1274$. Thus, the effect of the metric tensor on the residual zonal flow levels is very weak. We consider that this is because the ripple effect of the perpendicular wavenumber Eq.(30) for the GKV-X case with $g^{\rho\rho}$, which is plotted in Fig.1, is blinded with taking the flux surface average to determine the residual zonal flow potential that loses the poloidal-angle-dependent components associated with the geodesic acoustic mode (GAM) oscillations. Regarding the short-time response of the zonal flow potential, the finite gyroradius effects (due to $k_\perp\rho_{\rm i}$) on the frequency and the damping rate of the GAM are weaker than the effects of the Fourier spectrum of the confinement field strength as theoretically shown in Ref. [31]. In the present paper, the difference between the field strength structures used in the GKV and the GKV-X calculations is quite small as seen in Fig.2-(a). Therefore, the behaviors of the zonal flow response shown by both codes have only slight differences for the present case.

5 Conclusions

In this paper, we reported development of the new gyrokinetic Vlasov simulation code, GKV-X, which is applicable to non-axisymmetric configuration such as the LHD. The GKV-X code is designed to accurately deal with the effects of complicated geometry and helical ripple components of the confinement field, while the original GKV code uses the model confinement field for the geometry based on the large aspect ratio approximation. The new code includes full information about the metric tensor, the Jacobian, and the Fourier components of the helical field obtained from the VMEC equilibrium calculation. We performed the benchmark test of the GKV-X with the GKV calculations in the core plasma region of the standard LHD configuration. In the simulations of the linear ITG instability, we have found that the effects of full geometry and the helical ripples are enhanced for the higher poloidal wave numbers through the finite gyroradius effect and the magnetic drift frequency. The collisionless damping of the zonal flow potential is also examined, where the geometrical effects on the zonal flow show little differences between both codes. Thus, we can conclude that the GKV calculation with model helical field is useful especially for the phenomena with the long wavelengths in the standard LHD configuration with relatively small helical ripple components. However, we should mention that above benchmark tests are made for a core plasma region at $\rho = 0.6$, where the GKV simulations can be relatively appropriate for the investigation of the ITG modes and the zonal flows. Therefore, the GKV-X code can be a powerful tool to examine the effects of the full geometry and helical ripples on the ITG modes and the zonal flows, if we extend the simulation region to the edge region of the LHD plasmas where the geometrical effects are expected to appear more remarkably. This is because there exists strongly distorted magnetic surfaces and more complicated helical ripple components in the edge region.

The gyrokinetic simulation including the full effects of the complicated three-dimensional magnetic field is useful for quantitative investigation of the ITG

modes and the zonal flows in the helical systems. The GKV-X code enables us to study the ITG modes and the zonal flows in various types of field configurations, and to make comparison with the experimental data, of which results will be reported elsewhere.

Acknowledgment

One of authors (M. N.) appreciate Dr. S. Satake for useful information about the LHD equilibrium and the VMEC/NEWBOZ code. This work is supported in part by the Japanese Ministry of Education, Culture, Sports, Science and Technology, Grant No. 21560861, and in part by the NIFS Collaborative Research Program, NIFS09KTAL022, NIFS08KDAD008, NIFS08KTAL006 and NIFS08KNXN14.

[1] W. Horton, Rev. Mod. Phys. **71**, 735 (1999).
[2] P. H. Diamond, S.-I. Itoh, K. Itoh and T. S. Hahm, Plasma Phys. Control. Fusion **47**, R35 (2005).
[3] K. Itoh, S.-I. Itoh, P. H. Diamond and A. Fujisawa, Phys. Plasmas **13**, 055502 (2006).
[4] A. Fujisawa, Nucl. Fusion **49**, 013001 (2009).
[5] V. Kornilov, R. Kleiber, R. Hatzky, L. Villard and G. Jost, Phys. Plasmas **11**, 3196 (2004).
[6] T.-H. Watanabe, H. Sugama and S. Ferrando-Margalet, Phys. Rev. Lett. **100**, 195002 (2008).
[7] T.-H. Watanabe, H. Sugama and S. Ferrando-Margalet, Nucl. Fusion **47**, 1383 (2007).
[8] S. Ferrando-Margalet, H. Sugama and T.-H. Watanabe, Phys. Plasmas **14**, 122505 (2007).
[9] P. Xanthopoulos, F. Merz, T. Görler and F. Jenko, Phys. Rev. Lett. **99**, 035002 (2007).
[10] H. Sugama, T.-H. Watanabe and S. Ferrando-Margalet, Plasma Fusion Res. **3**, 041 (2008).
[11] T.-H. Watanabe and H. Sugama, Nucl. Fusion **46**, 24 (2006).
[12] O. Motojima, N. Ohyabu, A. Komori, O. Kaneko, H. Yamada, K. Kawahata, Y. Nakamura, K. Ida, T. Akiyama, N. Ashikawa, W. A. Cooper, A. Ejiri, M. Emoto, N. Ezumi, H. Funaba, A. Fukuyama, P. Goncharov, M. Goto, H. Idei, K. Ikeda, S. Inagaki, M. Isobe, S. Kado, H. Kawazome, K. Khlopenkov, T. Kobuchi, K. Kondo, A. Kostrioukov, S. Kubo, R. Kumazawa, Y. Liang, J. F. Lyon, A. Mase, S. Masuzaki, T. Minami, J. Miyazawa, T. Morisaki, S. Morita, S. Murakami, S. Muto, T. Mutoh, K. Nagaoka, Y. Nagayama, N. Nakajima, K. Nakamura, H. Nakanishi, K. Nariahara, Y. Narushima, K. Nishimura, N. Nishino, N. Noda, T. Notake, H. Nozato, S. Ohdachi, Y. Oka, H. Okada, S. Okamura, M. Osakabe, T. Ozaki, B. J. Peterson, A. Sagara, T. Saida, K. Saito, S. Sakakibara, M. Sakamoto, R. Sakamoto, M. Sasao, K. Sato, M. Sato, T. Seki, T. Shimozuma, M. Shoji, H. Suzuki, Y. Takeiri, N. Takeuchi, N. Tamura, K. Tanaka, M. Y. Tanaka, Y. Teramachi, K. Toi, T. Tokuzawa, Y. Tomota, Y. Torii, K. Tsumori, K. Y. Watanabe, T. Watari, Y. Xu, I. Yamada, S. Yamamoto, T. Yamamoto, M. Yokoyama, S. Yoshimura, Y. Yoshimura, M. Yoshinuma, N. Asakura, T. Fujita, T. Fukuda, T. Hatae, S. Higashijima, A. Isayama, Y. Kamada, H. Kubo, Y. Kusama, Y. Miura, T. Nakano, H. Ninomiya, T. Oikawa, N. Oyama, Y. Sakamoto, K. Shinohara, T. Suzuki, H. Takenaga, K. Ushigusa, T. Hino, M. Ichimura, Y. Takas, F. Sano, H. Zushi, T. Satow, S. Imagawa, T. Mito, I. Ohtake, T. Uda, K. Itoh, K. Ohkubo, S. Sudo, K. Yamazaki, M. Matsuoka, Y. Hamada, and M. Fujiwara, Nucl. Fusion **43**, 1674 (2003).
[13] H. Yamada, A. Komori, N. Ohyabu, O. Kaneko, K. Kawahata, K. Y. Watanabe, S. Sakakibara, S. Murakami, K. Ida, R. Sakamoto, Y. Liang, J. Miyazawa, K. Tanaka, Y. Narushima, S. Morita, S. Masuzaki, T. Morisaki, N. Ashikawa, L. R. Baylor, W. A. Cooper, M. Emoto, P. W. Fisher, H. Funaba, M. Goto, H. Idei, K. Ikeda, S. Inagaki, N. Inoue, M. Isobe, K. Khlopenkov, T. Kobuchi, A. Kostrioukov, S. Kubo, T. Kuroda, R. Kumazawa, T. Minami, S. Muto, T. Mutoh, Y. Nagayama, N. Nakajima, Y. Nakamura, H. Nakanishi, K. Narihara, K. Nishimura, N. Noda, T. Notake, S. Ohdachi, Y. Oka, M. Osakabe, T. Ozaki, B. J. Peterson, G. Rewoldt, A. Sagara, K. Saito, H. Sasao, M. Sasao, K. Sato, M. Sato, T. Seki, H. Sugama, T. Shimozuma, M. Shoji, H. Suzuki, Y. Takeiri, N. Tamura, K. Toi, T. Tokuzawa, Y. Torii, K. Tsumori, T. Watanabe, I. Yamada, S. Yamamoto, M. Yokoyama, Y. Yoshimura, T. Watari, Y. Xu, K. Itoh, K. Matsuoka, K. Ohkubo, T. Satow, S. Sudo, T. Uda, K. Yamazaki, O. Motojima, and M. Fujiwara, Plasma Phys. Controlled Fusion **43**, A55 (2001).
[14] T. Kuroda and H. Sugama, J. Phys. Soc. Jpn. **70**, 2235 (2001).
[15] P. Xanthopoulos and F. Jenko, Phys. Plasmas **13**, 092301 (2006).
[16] P. Xanthopoulos, W. A. Cooper, F. Jenko, Yu. Turkin, A. Runov, and J. Geiger, Phys. Plasmas **16**, 082303 (2009).
[17] H. E. Mynick, P. Xanthopoulos and A. H. Boozer, Phys. Plasmas **16**, 110702 (2009).
[18] S. P. Hirshman and O. Betancourt, J. Comput. Phys. **96**, 99 (1991).
[19] M. N. Rosenbluth and F. L. Hinton, Phys. Rev. Lett. **80**, 724 (1998).
[20] H. Sugama and T.-H. Watanabe, Phys. Rev. Lett. **94**, 115001 (2005).
[21] H. E. Mynick ans A. H. Boozer, Phys. Plasmas **14**, 072507 (2007).
[22] A. Mishchenko, P. Helander and A. Könies Phys. Plasmas **15**, 072309 (2008).
[23] O. Yamagishi and S. Murakami, Nucl. Fusion **49**, 045001 (2009).
[24] A. H. Boozer, Phys. Fluids **11**, 904 (1980).
[25] S. P. Hirshman and R. Morris (ORNL), private communication.
[26] M. A. Beer, S. C. Cowley and G. W. Hammett, Phys. Plasmas **2**, 2687 (1995).
[27] E. A. Frieman and L. Chen, Phys. Fluids **25**, 502 (1982).
[28] O. Yamagishi, M. Yokoyama, N. Nakajima and K. Tanaka, Phys. Plasmas **14**, 012505 (2007).
[29] G. Rewoldt, L.-P. Ku, W.M. Tang, H. Sugama, N. Nakajima, K.Y. Watanabe, S. Murakami, H. Yamada and W.A. Cooper, Nucl. Fusion **42**, 1047 (2002).
[30] T. Kuroda, H. Sugama, R. Kanno and M. Okamoto, J. Phys. Soc. Jpn. **69**, 2485 (2000).
[31] H. Sugama and T.-H. Watanabe, Phys. Plasmas **13**, 012501 (2006).

Table 1 Parameters at the flux surface $\rho = 0.6$ employed in the GKV code. The prime symbol means $A' = dA/d\rho$.

q_0	r_0/R_0	$\epsilon_{\rm t}$	$\epsilon_{\rm h}/\epsilon_{\rm t}$	$\epsilon_-/\epsilon_{\rm t}$	$\epsilon_+/\epsilon_{\rm t}$
1.9	0.0907	0.0878	0.9113	-0.2806	0.0498
$\hat{s}$	$\rho_0\epsilon'_{00}/\epsilon_{\rm t}$	$\rho_0\epsilon'_{\rm t}/\epsilon_{\rm t}$	$\rho_0\epsilon'_{\rm h}/\epsilon_{\rm t}$	$\rho_0\epsilon'_-/\epsilon_{\rm t}$	$\rho_0\epsilon'_+/\epsilon_{\rm t}$
-0.87501	0.1997	1.006	1.9486	-0.6452	0.070

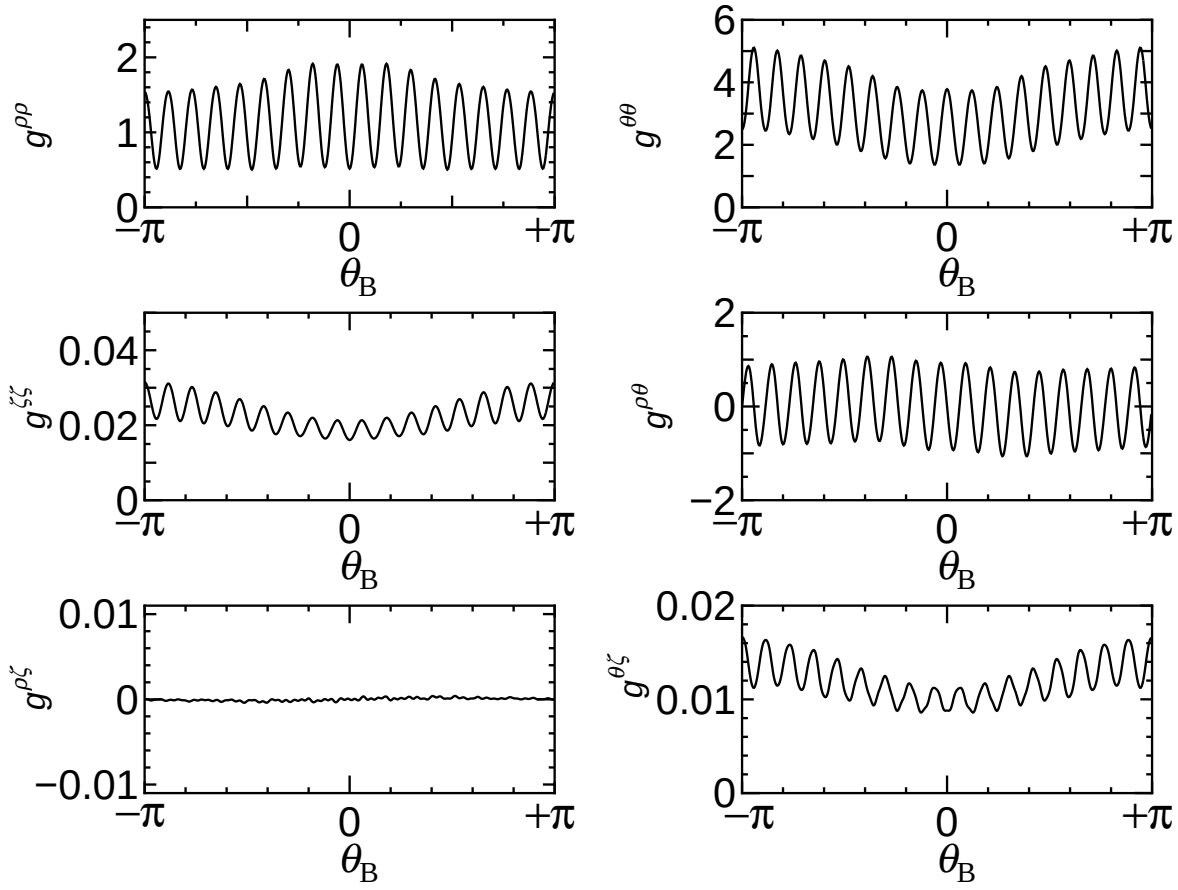

Fig. 1 Example of the contravariant components of the metric tensor, which is used for $k_\perp$ in Eq.(26), obtained by the VMEC/NEWBOZ outputted configuration at $\rho = 0.6$ in the Boozer coordinate system $\{\rho, \theta_{\rm B}, \zeta_{\rm B}\}$ with a fixed $\alpha = \zeta_{\rm B} - q_0\theta_{\rm B}$. Each component is in unit of a^{-2}.

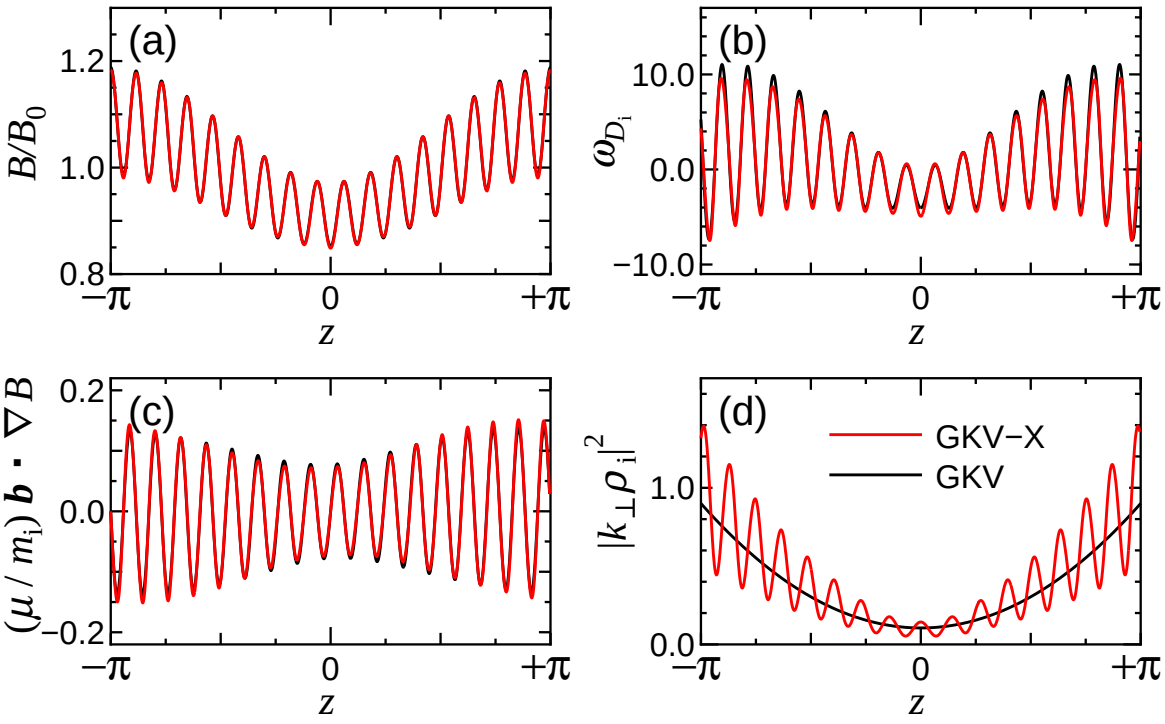

Fig. 2 Profiles of (a): the normalized magnetic field strength B/B_0, (b): the magnetic drift frequency $\omega_{\mathrm{D}i}$ normalized by $v_{\mathrm{t}i}L_n^{-1}$, (c): the mirror force term normalized by $v_{\mathrm{t}i}^2 L_n^{-1}$, and (d): the square of the normalized perpendicular wavenumber, $k_\perp \rho_i$. All profiles are evaluated at $\rho = 0.6$ and three plots except for (a) are calculated for $k_x \rho_i = 0$ and $k_y \rho_i = 0.324$. In (b) and (c), the magnetic moment is $\mu/(m_i \Omega_i B^{-1}) = 0.50\ v_{\mathrm{t}i} L_n$. Black and red curves show the results of the GKV and the GKV-X codes, respectively.

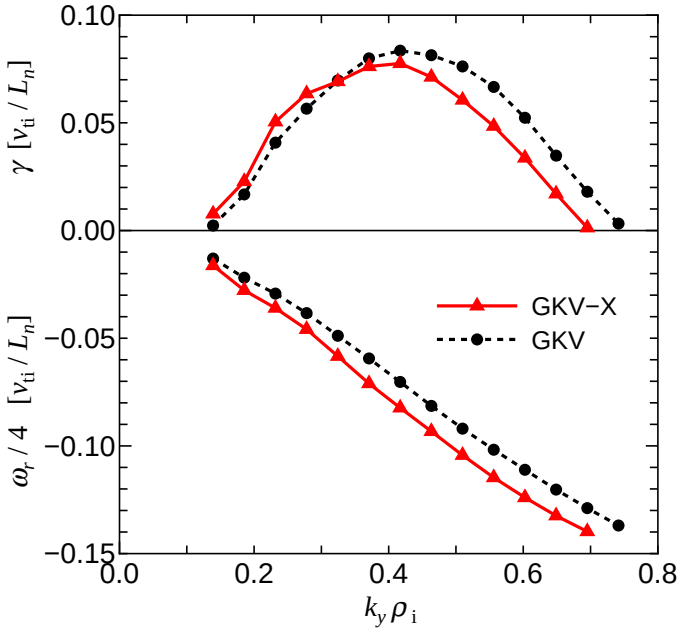

Fig. 3 Growth rates γ (top) and real frequencies ω_r (bottom) of the linear ITG mode, as functions of the normalized poloidal wave number $k_y\rho_i$, for the GKV simulation (black dashed lines with circles) and the GKV-X simulation (red solid lines with triangles).

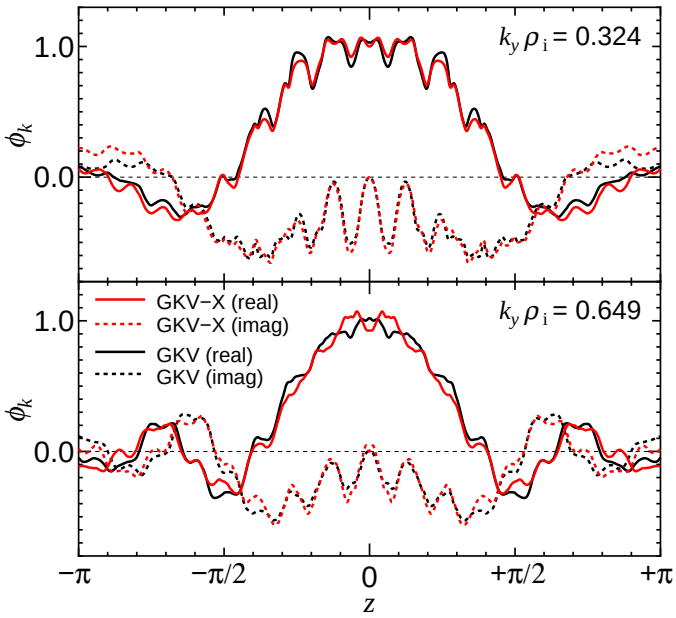

Fig. 4 Eigenfunctions of the electrostatic potential $\phi_k = \phi_r + i\phi_i$ along the parallel-to-field coordinate z for the linear ITG modes for $k_y\rho_i = 0.324$ (top) and $k_y\rho_i = 0.649$ (bottom) at $k_x = 0$. Real and imaginary parts of the eigenfunctions are plotted by the solid and dashed curves, respectively. Red and black curves express the results of the GKV-X and the GKV codes, respectively.

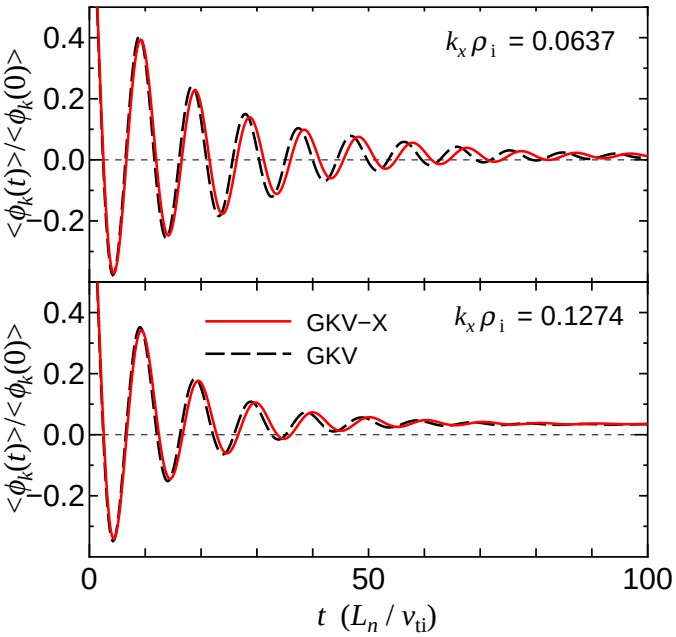

Fig. 5 Linear response of the zonal flow potential to the initial perturbation $\langle\phi_{k_\perp}(t)/\phi_{k_\perp}(0)\rangle$ for the GKV simulation with the model field (black dashed curves) and the GKV-X simulation with the VMEC field configuration (red solid curves). Here, the radial wave numbers are $k_x\rho_i = 0.0637$ (top) and $k_x\rho_i = 0.1274$ (bottom) for both codes.